



Neural-network-enhanced Fock-state tomography

Hsien-Yi Hsieh ¹, Yi-Ru Chen,¹ Mi-Mi Huang,¹ Jingyu Ning,¹ Hsun-Chung Wu ¹, Hua Li Chen,² Zi-Hao Shi,¹ Po-Han Wang,¹ Ole Steuernagel ¹, Chien-Ming Wu,¹ and Ray-Kuang Lee ^{1,2,3,4,*}

¹*Institute of Photonics Technologies, National Tsing Hua University, Hsinchu 30013, Taiwan*

²*Department of Physics, National Tsing Hua University, Hsinchu 30013, Taiwan*

³*Center for Theory and Computation, National Tsing Hua University, Hsinchu 30013, Taiwan*

⁴*Center for Quantum Science and Technology, Hsinchu 30013, Taiwan*



(Received 26 June 2024; accepted 15 October 2024; published 7 November 2024)

Even though heralded single-photon sources have been generated routinely through spontaneous parametric down conversion, vacuum and multiple photon states are unavoidably involved. With machine learning, we report the experimental implementation of photon number state tomography by directly estimating target parameters. Compared to the Hanbury Brown and Twiss measurements only with clicked events recorded, our neural-network-enhanced quantum-state tomography characterizes the photon number distribution for all possible photon number states from the balanced homodyne detectors. By using the histogram-based architecture, a direct parameter estimation on the negativity in Wigner's quasiprobability phase space is demonstrated. Such a fast, robust, and precise quantum-state tomography provides us a crucial diagnostic toolbox for the applications with incoherent mixture of Fock states.

DOI: [10.1103/PhysRevA.110.053705](https://doi.org/10.1103/PhysRevA.110.053705)

I. INTRODUCTION

Quantum-state tomography (QST) refers to the methodology in reconstructing the unknown quantum state with the acquired experimental data [1,2]. The maximum likelihood estimation (MLE) for QST finds the best-fitted probability distribution by treating the whole density matrix as the target of estimation [3–5]. As long as a sufficient computational effort is applied, MLE consistently yields a robust estimation, with the effectiveness in estimation strongly depending on the quantity of available data. Nowadays, QST has been successfully implemented as a diagnostic toolbox both for many-qubit (or qudits) systems in higher dimensions and for continuous variables in infinite dimensions [6–11].

However, MLE suffers from the overestimation problem as the required amount of measurements to reconstruct the quantum state exponentially increases with the number of involved modes. To overcome the overestimation problem in MLE, several modified algorithms are proposed, such as permutationally invariant tomography [12], quantum compressed sensing [13], tensor networks [14,15], generative models [16], and restricted Boltzmann machines [17], by assuming some physical restrictions imposed upon the state in question. Moreover, unavoidable coupling from the noisy environment makes the reconstructions on the density matrix with state degradation embedded, resulting in dealing with a nonsparse matrix in a larger Hilbert space.

With the power to find the best fit to arbitrarily complicated solutions, machine-learning (ML) enhanced QST has demonstrated its advantages in extracting complete information about the quantum states [17–21]. Furthermore, instead of

using the reconstruction model in training a truncated density matrix, with ML one may directly generate the target parameters with a supervised characteristic model [22]. Such a characteristic model-based ML-QST can be easily installed on edge devices such as a field programmable gate array (FPGA), serving as an in-line diagnostic toolbox for all possible applications. As an example, this ML-QST has also been applied to the reconstruction of Wigner current [23], demonstrating experimentally quantum dynamics in phase space in great detail. Compared to the time-consuming MLE, ML-QST paves the road toward a real-time and online QST [23,24].

With the benefits from the good properties of the Gaussian states, including vacuum and squeezed states, a neural network can directly analyze the *raw* data to obtain the first and second moments of the probability density function. By applying the well-developed methods in pattern recognitions [25–28], one can easily deal with various Gaussian states, producing a single scan QST in speeding up data acquisition and data processing [20]. Nevertheless, difficulties arise for such a relatively simple prediction map when non-Gaussian states are attacked. One may increase the number of neurons in dealing with non-Gaussian states, however the training process tends to cause an overfitting problem.

In the family of non-Gaussian states, single-photon Fock states play the core role as photonic qubits to carry quantum information encoded [29]. Although the request for an on-demand source of single photons has led to intense research into developing truly deterministic single-photon states, *heralded* single-photon sources can be easily generated through correlated pairs of photons, by detecting one photon (the heralding photon). After the first experimental observation in 1970 [30], nowadays, creating correlated photon pairs from spontaneous parametric down conversion (SPDC) has been routinely demonstrated with $\chi^{(2)}$ nonlinear crystals [31].

*Contact author: rkleee@ee.nthu.edu.tw

To characterize a single-photon Fock state, the common method is based on the second-order correlation function, $g^{(2)}(\tau)$, i.e., the Hanbury Brown and Twiss (HBT) interferometer [32–34]. The standard test for single-photon sources is a value of the second-order correlation function of the emitted field below 1/2 at zero time delay, i.e., $g^{(2)}(0) < 1/2$. However, this criterion alone provides no information regarding the amplitude of the single-photon contribution for general quantum states. In particular, a low-intensity light source always has a vacuum contribution in the quantum state of light, cloaking actual single-photon projection [35,36].

In addition to HBT measurements, nonclassical effects in the single-photon Fock states can be demonstrated in phase space [37], such as a negative value in the Wigner function [38]. Homodyne detection of the rotated quadratures provides an experimental implementation for the reconstruction on the Wigner function in phase space, through the inverse Radon problem [39,40]. Tomographic reconstruction of the single-photon states has been experimentally realized first with phase-randomized pulsed optical homodyne tomography [41–43], then with continuous temporal-mode matching [44], toward having real-time and complete temporal characterization of a single photon [45]. The development on homodyne tomography also provides a bridge between the single-photon and squeezed-vacuum states [46–48], as well as a methodology for various non-Gaussian states such as two-photon Fock states and optical cat states [49,50].

As the neural network predictor is often trained from some specific and limited amount of data, in this paper, we develop the machine-learning enhanced Fock-state tomography with the histogram-based architecture. Histogram-based approaches are often used to reduce the computational cost [51]. With an appropriately chosen bin width for the histogram, we demonstrate that the resulting quantum-state reconstruction can still keep fidelity high. Furthermore, with the capability of hybrid quantum-classical neural networks or quantum neural networks, the improvement in increased accuracy while reducing computational resources is also possible with quantum machine learning [52].

The paper is organized as follows: in Sec. II, we introduce our experimental setup to perform the homodyne detections on heralded single-photon Fock states, generated from SPDC process inside a bow-tie cavity. Then, the implementations of the histogram-based neural network are illustrated in Sec. III. The comparisons on the predicted photon number distributions from MLE and the neural network, also as a function of the SPDC pumping power, are given in Sec. IV. Moreover, a direct parameter prediction on the negativity is demonstrated, validating the feature extraction from our direct parameter estimations. Finally, we summarize this paper with some perspectives in Sec. V.

II. EXPERIMENTAL SETUP OF OUR SINGLE-PHOTON QUANTUM-STATE TOMOGRAPHY

The experimental setup for our heralded single-photon source and the quantum-state tomography is illustrated in Fig. 1. Here, the main laser source is a continuous-wave Nd:YAG laser at the wavelength of 1064 nm. This laser is split into two parts via a beam splitter: one serves as the local

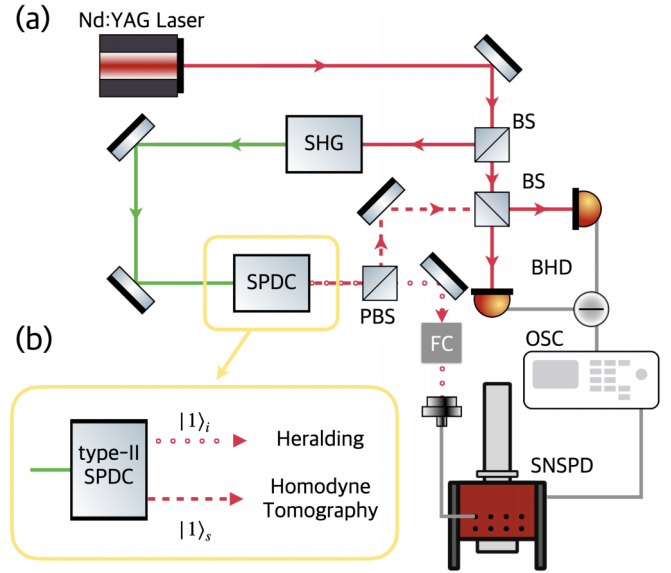


FIG. 1. (a) Our experimental setup to generate single-photon Fock-state tomography and its quantum-state tomography. (b) A simple schematic for generating heralded single-photon process by SPDC process. SHG, second harmonic generator; BHD, balanced homodyne detector; OSC, oscilloscope; SNSPD, superconducting nanowire single-photon detector; FC, filter cavities; BS, beam splitter; PBS, polarizing beam splitter.

oscillator beam for the balanced homodyne detector (BHD), while the other one serves as the pump field for the second harmonic generator (SHG). The SHG provides the frequency doubling at 532 nm, through a nonlinear crystal, i.e., periodically poled lithium niobate (PPLN), inside a bow-tie cavity. Then, the green light of the SHG signal is injected into another bow-tie cavity with a type-II PPLN crystal inside, in order to perform the SPDC process, which generates photon pairs in two orthogonal polarizations. The full width at half maximum of our SPDC cavity is 31.8 MHz and the free spectral range is 1.052 GHz. The outputs of orthogonal polarization beams, denoted as signal $|1\rangle_s$ and idler $|1\rangle_i$ photons in Fig. 1(b), are separated by a polarization beam splitter.

To ensure the mode matching in degenerate modes, the idler photon from the SPDC cavity is injected into a filter cavity (FC) system with 6.5 MHz in bandwidth. This FC system is composed of a triangle cavity and two Fabry-Pérot cavities. The detection on idler photons is performed by a superconducting nanowire single-photon detector (SNSPD). Finally, the SNSPD triggers the BHD to record the signal photons. As the Fock states are phase independent, we do not perform the measurement on rotated quadratures. The extracted quadrature data are obtained by integrating the temporal mode function on the experimental data, i.e.,

$$\hat{X}_i = \int_{-\infty}^{\infty} f(t) \hat{x}_i(t) dt,$$

with \hat{x}_i being the i th measurement data from the BHD. Here, the temporal mode function $f(t) = \sqrt{\pi\gamma} e^{-\pi\gamma|t-t_c|}$ is described by the center time for a trigger event t_c , with the decay rate of SPDC, denoted as γ .

In Fig. 2, we report our measured data on the second-order correlation function at zero time delay, $g^{(2)}(0)$, as a function of

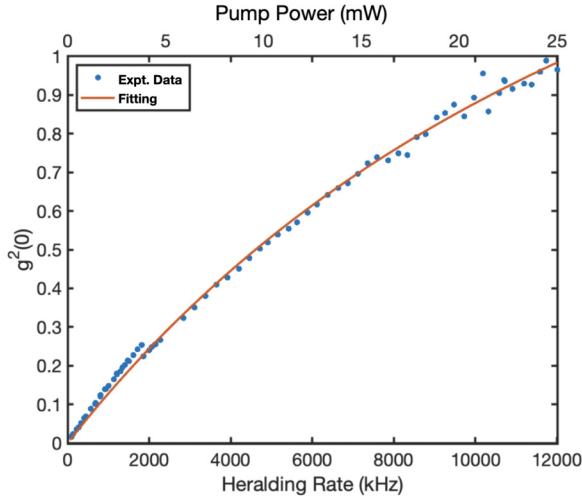


FIG. 2. Measured data on the second-order correlation function, $g^{(2)}(0)$, as a function of the recorded heralding rate in kHz, with the corresponding pump power labeled (on top) in mW.

the recorded heralding rate from the detection on the heralding idler photon into SNSPD. At the same time, the corresponding pump power (in mW) into the SPDC cavity is also depicted. One can see clearly that our single-photon source demonstrates $g^{(2)}(0) < 1/2$ when the pump power is smaller than 10 mW, or with the heralding rate about 4000 kHz (4 MHz). Note that due to different experimental runs, a slight jump in the measured data below and above 2 MHz heralding rate is recorded from the realignment of the setup.

In addition to the second-order correlation function, we also perform the quantum-state tomography for the heralded single-photon state with the homodyne detection scheme. In Fig. 3(a), a typical time sequence of our noisy single-photon source is demonstrated from our experimental raw data measured from the oscilloscope. Our BHD output is then integrated after convolution with a double-decayed (two time constants) temporal mode function, along with a detection correction treatment (in the reconstruction algorithm) that assumes a detection efficiency of 92%, which is composed of the quantum efficiency of photodiodes (99%), homodyne visibility efficiency (96%), and the circuit noise of homodyne detection (97%).

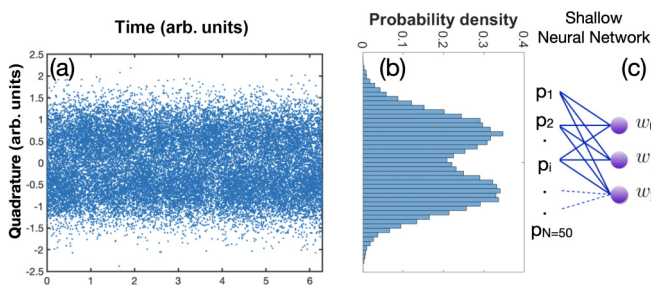


FIG. 3. (a) The time sequence of recorded BHD raw quadrature data measured from the oscilloscope. Here, the SPDC pump power is 3 mW. (b) The histogram of the corresponding probability density distribution, p_i ($i = 1 \dots N$). (c) With $N = 50$ inputs, a shallow neural network is applied to generate directly the predicted probability for different photon numbers w_n , with $n = 0, 1, 2$.

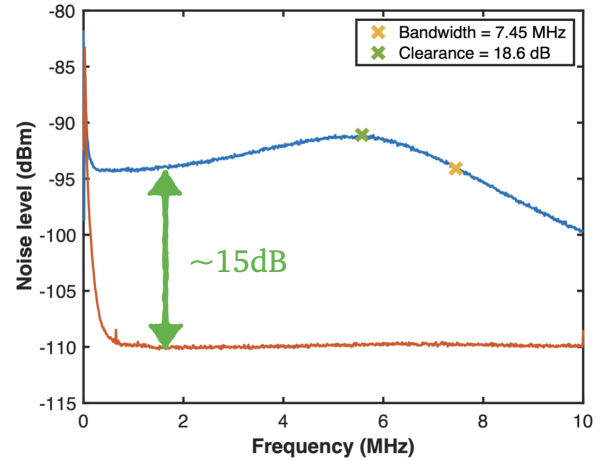


FIG. 4. Measured noise level in dB m of our BHD. Here, the spectrum for dark noise is depicted in red color, up to 10 MHz. When the local oscillator is operated at 30 mW, the spectrum of noise level is depicted in blue color, illustrating a maximum clearance of 18.6 dB, along with a 3-dB bandwidth up to 7.45 MHz.

To make sure the measured noise level is not contaminated, our homodyne detectors are designed with a high common mode rejection ratio of more than 80 dB [53]. As shown in Fig. 4, when the local oscillator is operated at 30 mW the spectrum of the noise level depicted in blue color demonstrates a clearance of higher than 15 dB (with a maximum value of 18.6 dB). However, our BHD only supports a 3-dB bandwidth up to 7.45 MHz.

In the following, by considering the limit in our BHD bandwidth, we analyze the SPDC pump power up to 3 mW (or the heralding rate lower than 2 MHz) on our Fock-state tomography with machine learning. This operation condition also reflects the scenario when the influence of vacuum significantly enters into the actual single-photon projection, denoted as the low-intensity limit.

III. HISTOGRAM-BASED MACHINE-LEARNING ENHANCED FOCK-STATE TOMOGRAPHY

Before introducing the histogram-based machine-learning architecture, we conduct several tests on Fock-state tomography by applying our previously developed convolution neural network for quantum-state tomography with simulated *raw* quadrature data [20]. As our goal is focusing on building a lightweight inference system which can be embedded into quantum optics experiments, working on *raw* quadrature data needs much more computation effort in dealing with complicated datasets. Instead, we construct histograms to reduce the input data size, as well as the required computational cost.

To reconstruct the quantum state in our SPDC experiment, the corresponding tomographic datum is the recorded event from our homodyne measurement, i.e.,

$$p(X) = \sum_{n=0}^{\infty} w_n \frac{1}{\pi^{1/2} 2^n n!} H_n^2(X) e^{-X^2}, \quad (1)$$

with the Hermite polynomial $H_n(X)$. Here, we already expand the probability probability distribution in Fock (photon

number) basis, with X being the value of the rotated quadrature and w_n being the photon number probability (weighting factor). As the Fock states are independent of the quadrature phase, we also apply the phase-average measurement [39–45] to our homodyne data. Tomographic reconstruction here is to estimate the photon number distributions w_n from the measured quadrature data X .

By checking all the experimental data, we first set the quadrature value between -3.2 and $+3.2$ as our range. Then, we divide this closed interval $[-3.2, 3.2]$ in the quadrature into 50 subintervals (bins) [see Fig. 3(b)]. The relative frequency of the i th bin is calculated by $f_i = \frac{N_i}{N}$, with N_i denoting the counts in the i th bin and N being the total counts in the quadrature axis. We want to remark that in our numerical experiments $N = 50$ bins (subintervals) are enough to achieve good results.

The relative frequency of the i th bin, f_i , is used to estimate the value of probability density defined on sampled quadrature values \hat{X}_i :

$$\frac{f_i}{\Delta X} \simeq p_i(\hat{X}_i), \quad i = 1 \dots N. \quad (2)$$

Here, ΔX is the length of each bin and \hat{X}_i is a specific point in the i th bin. With a uniform grid on X , the estimated value of probability density p_i is illustrated in Fig. 3(b). After this binning process, our tomographic problem now is transferred to predict w_n from the estimated value p_i defined on the discrete grid \hat{X}_i . When the number of input quadratures is large enough, the relative frequency converges to the probability, which enables a good approximated value of probability density p_i . Otherwise, errors occur in the binning process.

Here, for the mock data, one can calculate the probability density function $p(x)$ of the quadrature for a given value of w_n , by using Eq. (1). Then, we divide the quadrature axis into numerous bins and use the midpoint value of each quadrature bin to compute the probability density value, obtaining $p_i = p(x_i)$ for the training data, with i representing different bins. Collecting different w_n and their corresponding p_i values constitutes our training dataset.

Sets of more than 10 000 mock data on noisy single-photon experiments are prepared, including different percentages of single-photon and vacuum states [41–45]. We also explored various model architectures to implement raw-data (quadrature) based neural networks, and optimized the loss function as low as possible. Subsequently, we use this test dataset to evaluate the performance of these raw-data based neural networks.

However, the inferred average fidelity on 10 000 samples in these testing datasets is limited to 0.96 and even the input dimensions are up to 10 000. One possible solution to improve the fidelity is to apply advanced machine-learning architectures or to perform complex hyper parameter adjustments. These considerations also led us to adopt the histogram-based method, aiming to develop a lightweight network with high inference accuracy. The machine-learning model architecture is designed and optimized for noisy squeezed states environments but trained on non-Gaussian data.

In Fig. 3(c), the schematic of this histogram-based neural network for Fock-state QST is illustrated. Here, we apply a shallow neural network for 50 inputs from the

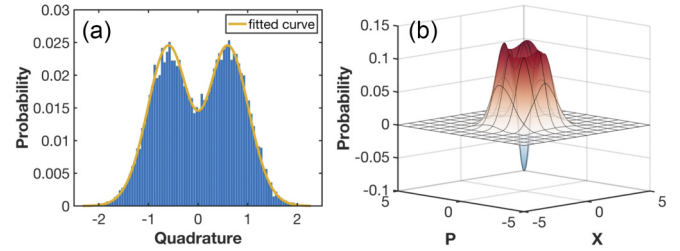


FIG. 5. (a) The measured probability density in the quadrature (X) from homodyne tomography data, with SPDC pump power at 3 mW. (b) The corresponding Wigner distribution function in the phase space. Here, the fitting curve for the probability density (in yellow color) is fitted by Eq. (4) with $\eta = 0.631$.

histogram-based inputs, i.e., the estimated values of quadrature probability density p_i . Our learning task is to build a map supporting a multiple instance setting:

$$p_i \rightarrow w_n. \quad (3)$$

Then, the outputs can generate directly the predicted probability for different photon numbers w_n .

To train our prediction map inferring different quantum states from various tomographic data, we feed the machine with well-prepared training dataset $\{p_i^k, w_n^k\}$. Here the index k counts for different instances which describe specific quantum states. In this learning task, we use a 10 000-data training dataset ($k = 10\,000$) and another 10 000 testing data with different weighting values of w_0 , w_1 , and w_2 , i.e., vacuum, single-photon, and two-photon Fock states, respectively. A uniform distribution in $[0, 1]$ is sampled. Furthermore, by considering the low-intensity condition in our SPDC experiments, we let $w_0 + w_1 + w_2 = 1$ without other multiphoton events. With the simulated data as the ground truth, our histogram-based neural network can ensure the average fidelity higher than 0.999 with 10 000 instances in testing datasets.

In our Fock-state QST, we also remark that the prediction map can be built only with a shallow neural network [see Fig. 3(c)]. Additional hidden layers are not needed here. We also perform the numerical test confirming that the neural network can maintain a good performance without any introduction of nonlinear activation functions. In the training process, we train ten epochs such that the mean-squared loss of both training and testing data decreases to 10^{-7} . The optimization process employs the ADAM optimizer with default hyperparameter settings, including a learning rate of 0.01.

IV. RESULTS AND DISCUSSIONS

A. Photon number distribution

To verify the validity of our histogram-based QST, first we compare directly with the measured probability density in the quadrature (X) from homodyne tomography data. As shown in Fig. 5(a), with the SPDC pump power at 3 mW, the recorded homodyne data illustrate clearly a non-Gaussian probability distribution. By assuming the light field has the form

$$\rho = (1 - \eta)|0\rangle\langle 0| + \eta|1\rangle\langle 1|,$$

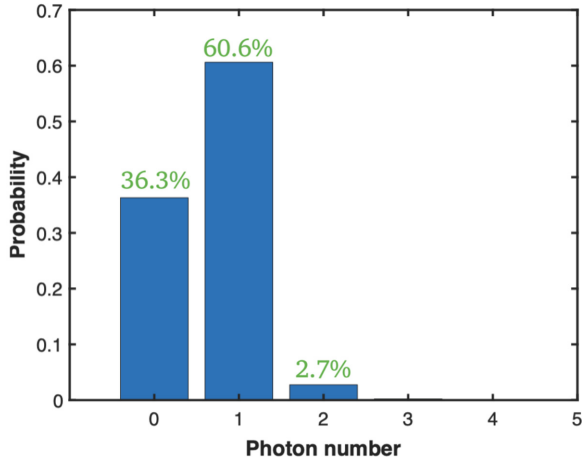


FIG. 6. The predicted probability distribution generated from our histogram-based QST from the same measured homodyne tomography data shown in Fig. 5(a), with SPDC pump power at 3 mW. Here, we have $w_0 = 0.363$, $w_1 = 0.606$, and $w_2 = 0.027$, corresponding to vacuum, single-photon, and two-photon Fock states, respectively.

as a noisy single-photon state $|1\rangle$ coupled to the vacuum $|0\rangle$, with the weighting factor η [41], the corresponding probability distribution function has the form

$$P(X; \eta) = \sqrt{\frac{2}{\pi}} [1 - \eta(1 - 4X^2)] e^{-2X^2}, \quad (4)$$

which gives the best fitting curve depicted in yellow color [see Fig. 5(a)], with $\eta = 0.631$.

With the Wigner transform, $\mathcal{W}[\hat{O}](x, p) = \int_{-\infty}^{\infty} dy O(x - \frac{y}{2}, x + \frac{y}{2}) e^{\frac{i}{\hbar}py}$ for a single-mode operator given in coordinate representation $\langle x - y | \hat{O} | x + y \rangle = O(x - y, x + y)$ [54,55], in Fig. 5(b) we show the corresponding Wigner distribution function in the phase space. A dip in the origin can be clearly seen, representing the negativity in Wigner's quasiprobability distribution as a signature of single-photon Fock states.

In Fig. 6, with the same measured homodyne tomography data shown in Fig. 5(a), i.e., the SPDC pump power at 3 mW, we show the predicted probability distribution generated from our histogram-based QST. Here, in addition to vacuum state $|0\rangle$ and single-photon Fock state $|1\rangle$, we also take possible two-photon Fock state $|n=2\rangle$ into consideration. The resulting photon number distribution gives $w_0 = 0.363$, $w_1 = 0.606$, and $w_2 = 0.027$, corresponding to vacuum, single-photon, and two-photon Fock states, respectively. The discrepancy between the direct fitting and our histogram-based QST [see Figs. 5(a) and 6] comes from the small portion in the two-photon Fock states.

As a benchmark, in Fig. 7 we also apply MLE method to verify the experimental data at different SPDC pump power. Here, both MLE and neural network generate a tiny value for the three-photon Fock state, i.e., $w_3 < 10^{-13}$, confirming that at most only up to w_2 (corresponding to two-photon Fock states) is non-negligible. With an increment in the SPDC pump power, the coefficient w_1 for single-photon Fock states increases, while the coefficient w_0 for vacuum states decreases. As shown in Fig. 7, both approaches exhibit almost the same curve, thereby indicating the equivalence and

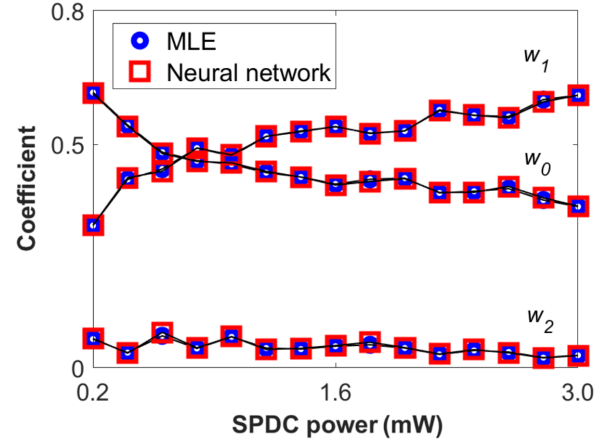


FIG. 7. Photon number distributions (w_0 , w_1 , and w_2) vs different SPDC pump power, compared with two different methods: maximum likelihood estimation (MLE) in circles and our histogram-based neural network in squares. For the histogram-based neural network, the input bin number is $N = 50$.

accuracy of these two estimations. To our surprise, at the same time our SPDC process inside a cavity also produces a small portion of two-photon Fock states, i.e., the average value of $w_2 = 0.044$ [41].

To avoid the overfitting problem in applying machine learning, we start with the simplest single-layer shallow neural network (only with 50 neurons). As we do not apply any complicated structures, the only factor change in the shallow neural network is the input size, which depends on how many discrete points are taken for the quadrature probability density. For the tests, we have increased the input size to 75 and 100, but the resulting fidelity generates 0.999 without showing significant improvements.

We want to remark that using a finer discretization also requires the increment in the number of input quadrature points. Experimental quadrature points ranging from 8000 to 20 000 are tested. We apply the the mean-square error (MSE) to compare the differences in inference results. All the tests give MSE on the order of 10^{-4} , indicating that the difference in photon components is very small. Fidelity checks also show no significant differences. As a comparison, we also apply the convolutional neural network architecture developed for squeezed states [20], to our single-photon experiments. However, the resulting fidelity can only achieve 0.95 due to the intrinsic overfitting problem by applying Gaussian states to map non-Gaussian Fock states. In other words, more data need to be obtained in the experiment, which reduces the overall tomographic reconstruction efficiency due to the speed of data collection. In our single-photon experiment, even though we only collected 8000 quadrature points, our current setting can achieve the target, which is also verified with the maximum likelihood estimation.

B. Direct parameter estimation

In addition to the photon number probability estimation, our histogram-based neural network can also predict directly the target parameters, without the reconstruction on the full quantum state. Here, we focus on the negativity in Wigner's

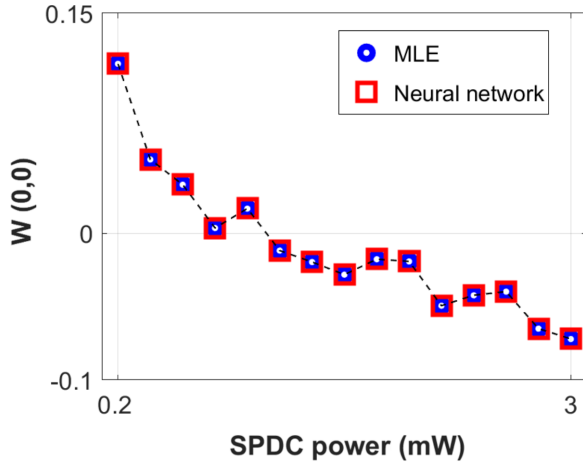


FIG. 8. Negativity in the Wigner function, $W(0,0)$, vs different SPDC pump power, compared with two different methods: maximum likelihood estimation (MLE) in squares and our histogram-based neural network in squares. For MLE, $W(0,0)$ is calculated after the reconstruction on the quantum state; the neural network directly estimates $W(0,0)$ by Eq. (5) from the quadrature histogram.

quasiprobability distribution, which manifests the most non-classical signature of single-photon Fock states. Analytically, the value in the origin of Wigner function $W(0,0)$ has the form

$$W(0,0) = \frac{1}{\pi} \sum_{n=0}^2 (-1)^n w_n L_n(0), \quad (5)$$

with the Laguerre polynomial $L_n(x)$ [38]. In Fig. 8, we illustrate the powerful feature in our histogram-based neural network by directly inferring the negativity in the Wigner function, $W(0,0)$, versus different SPDC pump power. Here, we also compare the results generated from two different methods: MLE-QST and our histogram-based neural network. It is noted that in MLE, $W(0,0)$ is calculated after the reconstruction on the quantum state. Nevertheless, our neural network directly estimates $W(0,0)$ directly by using Eq. (5) from the quadrature histogram. As one can see, again, our ML parameter estimation gives almost the same results as that from MLE.

By considering SPDC experiments in the low-intensity limit, the condition to have a negative value in $W(0,0)$ happens at $w_1 = 0.5$, corresponding to our SPDC pump power at 0.8 mW. As shown in Fig. 8, our histogram-based neural network, also confirmed by MLE, precisely estimates the negativity that happens when the SPDC pump power exceeds 0.8 mW.

As shown in Fig. 2, the value of $g^2(0)$ is smaller at low pump power, as only the “click” signals are recorded in the two detectors of the HBT interferometer. The vacuum states are not recorded in the HBT interferometer. However, as we reveal in Fig. 7, at low pump power, in our case below 3 mW,

there are always vacuum states (nonclick signals), which are totally discarded in the $g^2(0)$ measurements. Only with the quantum-state tomography, one can truly know the photon number distributions.

Last but not least, due to the perfect agreement between the results from MLE method and our histogram-based QST, we choose 50 bins as a good estimation. Unlike MLE method relying on the iteration algorithm, we can have a reusable prediction map from our neural network. This lightweight feature makes it easier to install such an inference function on edge devices like FPGA [56]. Most of the time-consuming task in our approach is the preprocessing, i.e., the histogram binning process, which takes about 0.01 s. However, it only takes about 3 ms to subsequently go through such a tiny 50×3 network for inference. The total time consumed is about $0.01 + 0.003$ s.

V. CONCLUSION

In summary, we develop a neural-network-enhanced Fock-state tomography and apply it to the heralding single-photon source from the SPDC process experimentally. Instead of tackling the raw quadrature data, which require a lot of computational cost but infer a limited fidelity up to 0.96, our histogram-based QST keeps the fidelity as high as 0.999. Moreover, target parameters, such as the photon number distribution and the negativity in the Wigner function, can be directly predicted, without dealing with the density matrix in a higher-dimensional Hilbert space.

Through the validation with the experimentally measured data acquired from the balanced homodyne detectors, perfect agreement to the results obtained by MLE is also clearly demonstrated. Compared to other methods to perform QST, such as directly from the detector statistics [57–59] and from the parity of the photon statistics [60,61], our machine-learning enhanced QST can be easily installed on edge devices such as FPGA as an in-line diagnostic toolbox for all the possible applications with single photons. Moreover, this fast and easy-to-install methodology helps us have a better understanding on quantum optics experiments with non-Gaussian states, such as two-photon Fock-state tomography [49], photon-added squeezed states [50], tomographic tests of Bell’s inequality [62], and the reconstruction of non-classicality [63].

ACKNOWLEDGMENTS

This work is partially supported by the National Science and Technology Council of Taiwan (No. 112-2123-M-007-001, No. 112-2119-M-008-007, No. 112-2119-M-007-006), Office of Naval Research Global, the International Technology Center Indo-Pacific (ITC IPAC) and Army Research Office, under Contract No. FA5209-21-P-0158, and the collaborative research program of the Institute for Cosmic Ray Research (ICRR) at the University of Tokyo.

[1] U. Leonhardt, *Measuring the Quantum State of Light* (Cambridge University Press, New York, 1997).

[2] A. I. Lvovsky and M. G. Raymer, Continuous-variable optical quantum-state tomography, *Rev. Mod. Phys.* **81**, 299 (2009).

- [3] K. Banaszek, Maximum-likelihood estimation of photon-number distribution from homodyne statistics, *Phys. Rev. A* **57**, 5013 (1998).
- [4] Z. Hradil, Quantum-state estimation, *Phys. Rev. A* **55**, R1561(R) (1997).
- [5] A. I. Lvovsky, Iterative maximum-likelihood reconstruction in quantum homodyne tomography, *J. Opt. B* **6**, S556 (2004).
- [6] U. L. Andersen, J. S. Neergaard-Nielsen, P. van Loock, and A. Furusawa, Hybrid discrete- and continuous-variable quantum information, *Nat. Phys.* **11**, 713 (2015).
- [7] D. Barredo, S. de Leseleuc, V. Lienhard, T. Lahaye, and A. Browaeys, An atom-by-atom assembler of defect-free arbitrary two-dimensional atomic arrays, *Science* **354**, 1021 (2016).
- [8] M. Endres, H. Bernien, A. Keesling, H. Levine, E. R. Anschuetz, A. Krajenbrink, C. Senko, V. Vuletic, M. Greiner, and M. D. Lukin, Atom-by-atom assembly of defect-free one-dimensional cold atom arrays, *Science* **354**, 1024 (2016).
- [9] J. Zhang, G. Pagano, P. W. Hess, A. Kyprianidis, P. Becker, H. Kaplan, A. V. Gorshkov, Z.-X. Gong, and C. Monroe, Observation of a many-body dynamical phase transition with a 53-qubit quantum simulator, *Nature (London)* **551**, 601 (2017).
- [10] N. Friis, O. Marty, C. Maier, C. Hempel, M. Holzäpfel, P. Jurcevic, M. B. Plenio, M. Huber, C. Roos, R. Blatt, and B. Lanyon, Observation of entangled states of a fully controlled 20-qubit system, *Phys. Rev. X* **8**, 021012 (2018).
- [11] B. Vlastakis, G. Kirchmair, Z. Leghtas, S. E. Nigg, L. Frunzio, S. M. Girvin, M. Mirrahimi, M. H. Devoret, and R. J. Schoelkopf, Deterministically encoding quantum information using 100-photon Schrödinger cat states, *Science* **342**, 607 (2013).
- [12] G. Tóth, W. Wieczorek, D. Gross, R. Krischek, C. Schwemmer, and H. Weinfurter, Permutationally invariant quantum tomography, *Phys. Rev. Lett.* **105**, 250403 (2010).
- [13] D. Gross, Y.-K. Liu, S. T. Flammia, S. Becker, and J. Eisert, Quantum state tomography via compressed sensing, *Phys. Rev. Lett.* **105**, 150401 (2010).
- [14] M. Cramer, M. B. Plenio, S. T. Flammia, D. Gross, S. D. Bartlett, R. Somma, O. Landon-Cardinal, D. Poulin, and Y.-K. Liu, Efficient quantum state tomography, *Nat. Commun.* **1**, 149 (2010).
- [15] B. P. Lanyon, C. Maier, M. Holzäpfel, T. Baumgratz, C. Hempel, P. Jurcevic, I. Dhand, A. S. Buyskikh, A. J. Daley, M. Cramer, M. B. Plenio, R. Blatt, and C. F. Roos, Efficient tomography of a quantum many-body system, *Nat. Phys.* **13**, 1158 (2017).
- [16] J. Carrasquilla, G. Torlai, R. G. Melko, and L. Aolita, Reconstructing quantum states with generative models, *Nat. Mach. Intell.* **1**, 155 (2019).
- [17] E. S. Tiunov, V. V. Tiunova, A. E. Ulanov, A. I. Lvovsky, and A. K. Fedorov, Experimental quantum homodyne tomography via machine learning, *Optica* **7**, 448 (2020).
- [18] J. Biamonte, P. Wittek, N. Pancotti, P. Rebentrost, N. Wiebe, and S. Lloyd, Quantum machine learning, *Nature (London)* **549**, 195 (2017).
- [19] S. Lohani, B. T. Kirby, M. Brodsky, O. Danaci, and R. T. Glasser, Machine learning assisted quantum state estimation, *Mach. Learn.: Sci. Technol.* **1**, 035007 (2020).
- [20] H.-Y. Hsieh, Y.-R. Chen, H.-C. Wu, H. L. Chen, J. Ning, Y.-C. Huang, C.-M. Wu, and R.-K. Lee, Extract the degradation information in squeezed states with machine learning, *Phys. Rev. Lett.* **128**, 073604 (2022).
- [21] S. Ahmed, C. Sanchez Muoz, F. Nori, and A. F. Kockum, Quantum state tomography with conditional generative adversarial networks, *Phys. Rev. Lett.* **127**, 140502 (2021).
- [22] H.-Y. Hsieh, J. Ning, Y.-R. Chen, H.-C. Wu, H. L. Chen, C.-M. Wu, and R.-K. Lee, Direct parameter estimations from machine learning-enhanced quantum state tomography, *Symmetry* **14**, 874 (2022).
- [23] Y.-R. Chen, H.-Y. Hsieh, J. Ning, H.-C. Wu, H. L. Chen, Y.-L. Chuang, P. Yang, O. Steuernagel, C.-M. Wu, and R.-K. Lee, Experimental reconstruction of Wigner phase-space current, *Phys. Rev. A* **108**, 023729 (2023).
- [24] A. Youssry, C. Ferrie, and M. Tomamichel, Efficient online quantum state estimation using a matrix-exponentiated gradient method, *New J. Phys.* **21**, 033006 (2019).
- [25] A. Krizhevsky, I. Sutskever, and G. E. Hinton, ImageNet classification with deep convolutional neural networks, in *Advances in Neural Information Processing Systems*, edited by F. Pereira, C. J. Burges, L. Bottou, and K. Q. Weinberger (Curran Associates, Red Hook, New York, 2012), Vol. 25, p. 1097.
- [26] K. He, X. Zhang, S. Ren, and J. Sun, Deep residual learning for image recognition, in *Proceedings of the 2016 IEEE Conference on Computer Vision and Pattern Recognition* (IEEE, New York, 2016).
- [27] G. Huang, Z. Liu, L. van der Maaten, and K. Q. Weinberger, Densely connected convolutional networks, in *Proceedings of the IEEE Computer Society Conference on Computer Vision and Pattern Recognition* (IEEE, New York, 2017), p. 2261.
- [28] S. Abdoli, P. Cardinal, and A. L. Koerich, End-to-end environmental sound classification using a 1D convolutional neural network, *Expert Syst. Applic.* **136**, 252 (2019).
- [29] M. D. Eisaman, J. Fan, A. Migdall, and S. V. Polyakov, Single-photon sources and detectors, *Rev. Sci. Instrum.* **82**, 071101 (2011).
- [30] D. Burnham and D. Weinberg, Observation of simultaneity in parametric production of optical photon pairs, *Phys. Rev. Lett.* **25**, 84 (1970).
- [31] O. Morin, V. D'Auria, C. Fabre, and J. Laurat, High-fidelity single-photon source based on a type II optical parametric oscillator, *Opt. Lett.* **37**, 3738 (2012).
- [32] R. Hanbury Brown and R. Q. Twiss, A test of a new type of stellar interferometer on sirius, *Nature (London)* **178**, 1046 (1956).
- [33] R. J. Glauber, The quantum theory of optical coherence, *Phys. Rev.* **130**, 2529 (1963).
- [34] E. C. G. Sudarshan, Equivalence of semiclassical and quantum mechanical descriptions of statistical light beams, *Phys. Rev. Lett.* **10**, 277 (1963).
- [35] P. Grünwald, Effective second-order correlation function and single-photon detection, *New J. Phys.* **21**, 093003 (2019).
- [36] J. R. Chavez-Mackay, P. Grünwald, and B. M. Rodríguez-Lara, Estimating the single-photon projection of low-intensity light sources, *Phys. Rev. A* **101**, 053815 (2020).
- [37] N. Lütkenhaus and S. M. Barnett, Nonclassical effects in phase space, *Phys. Rev. A* **51**, 3340 (1995).
- [38] C. Baune, J. Fiurášek, and R. Schnabel, Negative Wigner function at telecommunication wavelength from homodyne detection, *Phys. Rev. A* **95**, 061802(R) (2017).

- [39] M. Munroe, D. Boggavarapu, M. E. Anderson, and M. G. Raymer, Photon-number statistics from the phase-averaged quadrature-field distribution: Theory and ultrafast measurement, *Phys. Rev. A* **52**, R924(R) (1995).
- [40] S. M. Tan, An inverse problem approach to optical homodyne tomography, *J. Mod. Opt.* **44**, 2233 (1997).
- [41] A. I. Lvovsky, H. Hansen, T. Aichele, O. Benson, J. Mlynek, and S. Schiller, Quantum state reconstruction of the single-photon Fock state, *Phys. Rev. Lett.* **87**, 050402 (2001).
- [42] A. Zavatta, S. Viciani, and M. Bellini, Tomographic reconstruction of the single-photon Fock state by high-frequency homodyne detection, *Phys. Rev. A* **70**, 053821 (2004).
- [43] S. R. Huisman, N. Jain, S. A. Babichev, F. Vewinger, A. N. Zhang, S. H. Youn, and A. I. Lvovsky, Instant single-photon Fock state tomography, *Opt. Lett.* **34**, 2739 (2009).
- [44] H. Ogawa, H. Ohdan, K. Miyata, M. Taguchi, K. Makino, H. Yonezawa, J. I. Yoshikawa, and A. Furusawa, Real-time quadrature measurement of a single-photon wave packet with continuous temporal-mode matching, *Phys. Rev. Lett.* **116**, 233602 (2016).
- [45] Z. Qin, A. S. Prasad, T. Brannan, A. MacRae, A. Lezama, and A. I. Lvovsky, Complete temporal characterization of a single photon, *Light Sci. Appl.* **4**, e298 (2015).
- [46] N. Jain, S. R. Huisman, E. Bimbard, and A. I. Lvovsky, A bridge between the single-photon and squeezed-vacuum states, *Opt. Express* **18**, 18254 (2010).
- [47] N. B. Grosse, T. Symul, M. Stobińska, T. C. Ralph, and P. K. Lam, Measuring photon antibunching from continuous variable sideband squeezing, *Phys. Rev. Lett.* **98**, 153603 (2007).
- [48] J. C. López Carreño, E. Z. Casalengua, B. Silva, E. del Valle, and F. P. Laussy, Loss of antibunching, *Phys. Rev. A* **105**, 023724 (2022).
- [49] A. Ourjoumtsev, R. Tualle-Brouiri, and P. Grangier, Quantum homodyne tomography of a two-photon Fock state, *Phys. Rev. Lett.* **96**, 213601 (2006).
- [50] Y.-R. Chen, H.-Y. Hsieh, J. Ning, H.-C. Wu, H. L. Chen, Z.-H. Shi, P. Yang, O. Steuernagel, C.-M. Wu, and R.-K. Lee, Generation of heralded optical cat states by photon addition, *Phys. Rev. A* **110**, 023703 (2024).
- [51] J. L. E. Silva, S. Glancy, and H. M. Vasconcelos, Quadrature histograms in maximum-likelihood quantum state tomography, *Phys. Rev. A* **98**, 022325 (2018).
- [52] A. Melnikov, M. Kordzanganeh, A. Alodjants, and R.-K. Lee, Quantum machine learning: From physics to software engineering, *Adv. Phys. X* **8**, 2165452 (2023).
- [53] C.-M. Wu, S.-R. Wu, Y.-R. Chen, H.-C. Wu, and R.-K. Lee, Detection of 10 dB vacuum noise squeezing at 1064 nm by balanced homodyne detectors with a common mode rejection ratio more than 80 dB, in *Conference on Lasers and Electro-Optics*, OSA Technical Digest (Optica Publishing Group, 2019), p. JTu2A.38.
- [54] J. Hancock, M. A. Walton, and B. Wynder, Quantum mechanics another way, *Eur. J. Phys.* **25**, 525 (2004).
- [55] D. Cohen, Lecture notes in quantum mechanics, [arXiv:quant-ph/0605180](https://arxiv.org/abs/quant-ph/0605180).
- [56] H.-C. Wu, H.-Y. Hsieh, Y.-R. Chen, J. Ning, H. L. Chen, Z.-H. Shi, P. H. Wang, O. Steuernagel, C.-M. Wu, and R.-K. Lee, Implementation of model deployment on FPGA for the real-time machine learning based quantum state tomography (unpublished).
- [57] E. Fedotova, N. Kuznetsov, E. Tiunov, A. E. Ulanov, and A. I. Lvovsky, Continuous-variable quantum tomography of high-amplitude states, *Phys. Rev. A* **108**, 042430 (2023).
- [58] G. Zambra, A. Andreoni, M. Bondani, M. Gramegna, M. Genovese, G. Brida, A. Rossi, and M. G. A. Paris, Experimental reconstruction of photon statistics without photon counting, *Phys. Rev. Lett.* **95**, 063602 (2005).
- [59] P. R. Banner, D. Kurdak, Y. Li, A. Migdall, J. V. Porto, and S. L. Rolston, Number-state reconstruction with a single single-photon avalanche detector, *Optica Quantum* **2**, 110 (2024).
- [60] A. Royer, Wigner function as the expectation value of a parity operator, *Phys. Rev. A* **15**, 449 (1977).
- [61] K. Laiho, M. Avenhaus, K. N. Cassemiro, and Ch. Silberhorn, Direct probing of the Wigner function by time-multiplexed detection of photon statistics, *New J. Phys.* **11**, 043012 (2009).
- [62] M. D'Angelo, A. Zavatta, V. Parigi, and M. Bellini, Tomographic test of Bell's inequality for a time-delocalized single photon, *Phys. Rev. A* **74**, 052114 (2006).
- [63] S. Deleglise, I. R. Dotsenko, C. Sayrin, J. Bernu, M. Brune, J.-M. Raimond, and S. Haroche, Reconstruction of non-classical cavity field states with snapshots of their decoherence, *Nature (London)* **455**, 510 (2008).